FULL PAPER

Applied Organometallic Chemistry WILEY

Iron(III), copper(II), cadmium(II), and mercury(II) complexes of isatin carbohydrazone Schiff base ligand (H₃L): Synthesis, characterization, X-ray diffraction, cyclic voltammetry, fluorescence, density functional theory, biological activity, and molecular docking studies

Adel M. Younis[1] ⓘ | Mohammed M. El-Gamil[2] ⓘ | Tawfik H. Rakha[1] ⓘ |
Gaber M. Abu El-Reash[1] ⓘ

[1]Chemistry Department, Faculty of Science, Mansoura University, PO Box 70, Mansoura, Egypt

[2]Department of Toxic and Narcotic Drug, Forensic Medicine, Mansoura Laboratory, Medico-Legal Organization, Ministry of Justice, Mansoura, Egypt

Correspondence
Gaber M. Abu El-Reash, Chemistry Department, Faculty of Science, Mansoura University, Mansoura, PO Box 70, Mansoura, Egypt.
Email: gaelreash@mans.edu.eg

Mohammed M. El-Gamil, Department of Toxic and Narcotic Drug, Forensic Medicine, Mansoura Laboratory, Medico-Legal Organization, Ministry of Justice, Mansoura, Egypt.
Email: m_elgamil2004@yahoo.com

A series of some transition metal, Fe(III), Cu(II), Cd(II), and Hg(II), complexes with N',2-bis((Z)-2-oxoindolin-3-ylidene)hydrazine-1 carbohydrazide (H₃L) ligand have been synthesized, and their structures were elucidated based on their spectral analyses (Fourier transform infrared [FT-IR], ¹H nuclear magnetic resonance (NMR) and ¹³C NMR, UV-visible (UV-Vis), electron spin resonance (ESR), powder X-ray diffraction [XRD], and mass spectroscopy), elemental analyses, conductance, and magnetic susceptibility measurements. The structures of the H₃L ligand and its metal complexes were optimized using the DMol³ tool in the material studio package. The ligand behaves as binegative N^2O^3 pentadentate in [Fe(HL)(Cl)]·2H₂O complex, mononegative N^2O^3 pentadentate in [Cu(H₂L)(OAc)]·2H₂O complex, mononegative N^2O tridentate in [Cd(H₂L)₂]·H₂O complex, and finally, neutral N^2 bidentate in [Hg(H₃L)(Cl)₂]·2H₂O complex. Coats–Redfern and Horowitz–Metzger methods were used to estimate the various thermodynamic and kinetic parameters. Cyclic voltammetry of the ligand in the absence and presence of Cd(II) and Hg(II) ions was studied. Fluorescence studies were performed in DMSO and showed that Cu(II) ions quench the fluorescence spectrum of the free ligand, whereas Cd(II) ions enhance it. The in vitro antimicrobial activities of the free ligand and its complexes against different bacterial strains and fungi *Candida albicans* were screened using agar-disc diffusion techniques. The antioxidant potentials of the isolated compounds were also screened by employing SOD and ABTS free radical scavenging methods. Molecular docking studies were performed using Auto-Dock tools to predict the best binding mode and predominant binding interactions.

KEYWORDS
ABTS, ESR, florescence studies, molecular docking, XRD

1 | INTRODUCTION

For the first time, Schiff bases were described in 1864 by H. Schiff.[1,2] Hydrazones are considered a vital category of Schiff base compounds that have distinctive pharmaceutical applications as anti-inflammatory,[3] antimicrobial,[4] and anticonvulsing agents[5] and have diverse applications in numerous areas such as food and dyes industries, catalysis, analytical chemistry, and agrochemical industries.[6,7] The biological activity of the metal complex may be more prominent or lower than that of the metal ion or/and the ligand.[8,9] Syntheses of metal complexes with carbohydrazide and their Schiff base derivatives have inspired research topics in coordination chemistry for a long time.[10] Due to the preparatory accessibility and structural variety, the transition metal complexes of Schiff bases are the most significant stereochemical pattern in coordination chemistry.[11] Isatins are considered an important class of heterocyclic compounds as they have different activities like antimicrobial,[12] antibacterial, and antifungal activities.[13] In the current work, we would like to consider the chelating properties of N',2-bis((Z)-2-oxoindolin-3-ylidene) hydrazine-1 carbohydrazide (H_3L) towards Fe(III), Cu(II), Cd(II), and Hg(II) metal ions in details, covering structure elucidation, molecular modeling, the biological activities of the isolated compounds, changes observed in the fluorescence spectrum, cyclic voltammogram of the ligand upon addition of different metal ions, and molecular docking of the ligand and its complexes.

2 | EXPERIMENTAL

2.1 | Materials and methods

All the chemicals and solvents used (isatin, hydrazinecarbohydrazide, ethanol, diethyl ether, metal chlorides, and metal acetates) were purchased from normal business associations such as British Drug House (BDH) and Sigma-Aldrich and used as supplied without additional refinement. Fourier transform infrared (FT-IR), nuclear magnetic resonance (NMR), and UV-visible (UV-Vis) spectra were recorded employing Mattson 5000 FT-IR spectrophotometer (as KBr discs) within the range 4000–400 cm^{-1}, Bruker Avance 400 MHz, and Unicam UV-Vis spectrophotometer, respectively. The fluorescence emission spectral measurements were recorded using an Agilent Cary Eclipse Fluorescence spectrophotometer. Samples were excited at 480 nm in recording the fluorescence spectra. Carbon, hydrogen, and nitrogen content was estimated using a Perkin-Elmer CHN analyzer. The metal and chloride content was evaluated according to recorded methods.[14] Gas chromatography–mass spectrometry (GC–MS) spectra were recorded on a Varian Mat 311. EPR spectrum of [Cu(H_2L)(OAc)]·2H_2O complex was recorded using a Jeol JES-RE1X EPR device using the usual standard (DPPH). Thermal measurements (thermal gravimetric analysis [TGA]–differential thermal analysis [DTA]) were obtained using Shimadzu thermogravimetric analyzer DTG-60H in a nitrogen atmosphere (gas flow 20 ml min^{-1}) with a 10°C min^{-1} heating rate. Cyclic voltammetry measurements were obtained using DY2100 apparatus at 0.1, 0.01, 0.02, and 0.05 mV s^{-1} scan rates. Magnetic susceptibilities were estimated using a Sherwood magnetic balance. All measurements were done at room temperature.

2.2 | Preparation of H_3L ligand and its metal complexes

2.2.1 | Synthesis of H_3L ligand

A hot ethanolic solution of hydrazinecarbohydrazide (carbohydrazide) (1.8 g, 0.02 mol) was added to ethanolic solutions of isatin (5.9 g, 0.04 mol). The resulted mixture was refluxed at 70°C to 80°C for 3 h. The yellow, solid product resulted was filtered off, washed, and dried in a desiccator over CaCl$_2$ anhydrous.

2.2.2 | Synthesis of metal complexes

Individually, for each one of the complexes, four solutions of H_3L ligand (Figure 1) (0.5 g, 0.0015 mol) in 15-ml absolute ethanol were prepared and then for [Fe(HL)(Cl)]·2H_2O complex (Figure 2): (0.3 g, 0.0015 mol) of anhydrous FeCl$_3$, for [Cu(H_2L)(OAc)]·2H_2O complex (Figure 3): (0.26 g, 0.0015 mol) of Cu (CH$_3$COO)$_2$, for [Cd (H_2L)]·H_2O complex (Figure 4): (0.4 g, 0.0015 mol) of Cd (CH$_3$COO)$_2$·2H_2O, and for [Hg(H_3L)(Cl)$_2$]·2H_2O complex (Figure 5): (0.4 g, 0.0015 mol) of HgCl$_2$ were dissolved in 15-ml absolute ethanol and added drop by drop to the prepared ligand solutions. The resulted mixtures were reflexed at 60°C to 70°C for 6 h, and the resulted colored compounds were filtered, washed, and then dried over anhydrous CaCl$_2$.

2.3 | Molecular modeling

The isolated ligand and its complexes were optimized using DMol^3 code in the material studio program,[15–19] with the revising Perdew-Burke-Ernzerhof (RPBE) functional,[20] with the double numerical basis set with polarization functions (DNP).[21]
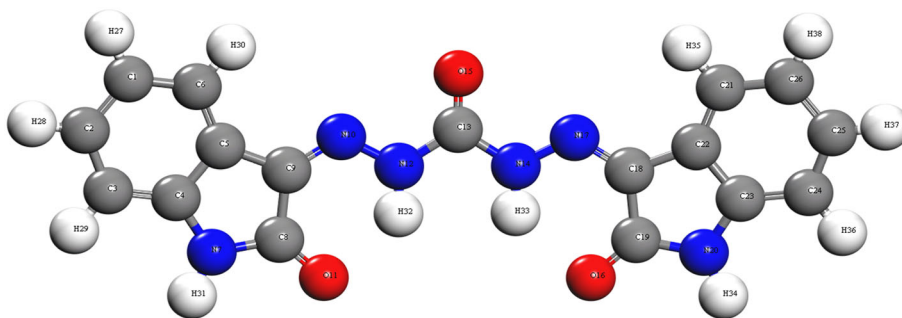
FIGURE 1 Molecular structure of H₃L ligand

FIGURE 2 Molecular structure of [Fe(HL)(Cl)]·2H₂O complex

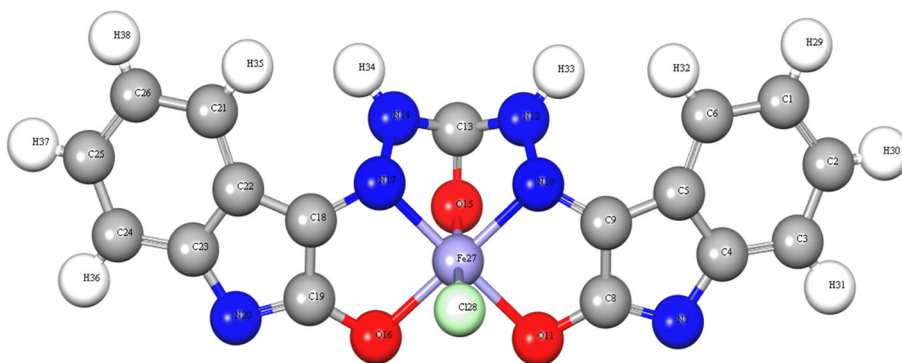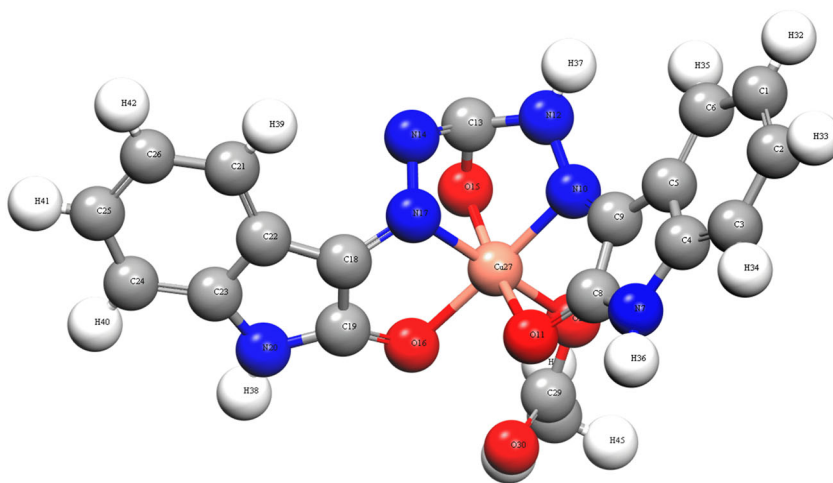**FIGURE 3** Molecular structure of [Cu(H₂L)(OAc)]·2H₂O complex

2.4 | Molecular docking

Molecular docking studies were used to give a suitable indication for the ligand–receptor interactions with the aid of computational methods. The Auto-Dock 4.2 and MGL 1.5.6 tools were used in docking studies.[22,23] The structures of *Escherichia coli*, *Bacillus subtilis*, *Staphylococcus aureus*, *Pseudomonas aeruginosa*, *Candida albicans*, and *xanthine oxidase* were obtained from a protein database (RCSB PDB) with ID: *1C14*, *4BPF*, *3BL6*, *3P3E*, *5V5Z*, and *1FIQ*, respectively.[24–29] Water molecules were eliminated, and hydrogen atoms were added. The grid box was put up with dimensions of $60 \times 60 \times 60$ Å and 0.375-Å grid spacing. Gasteiger charges were added utilizing the AD tools, and the Lamarckian genetic algorithm was used in looking up the ideal binding site of the ligand. The results obtained were analyzed using the BIOVIA DS visualizer software.[30]

2.5 | Biological applications

2.5.1 | Antimicrobial activity

The H_3L ligand and its metal complexes were all screened for their in vitro antimicrobial activity using the disc diffusion and agar diffusion methods.[31–33]
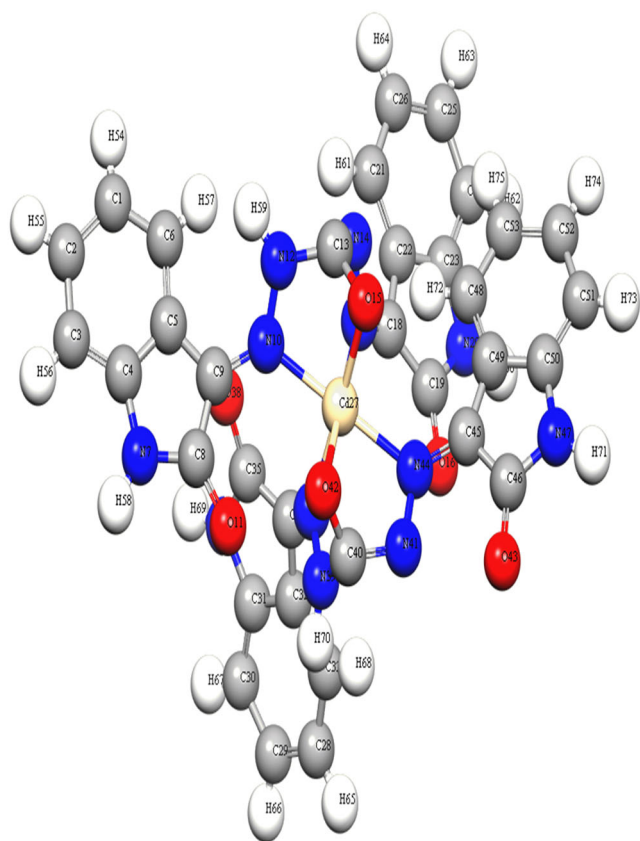
FIGURE 4 Molecular structure of [Cd(H$_2$L)$_2$]·H$_2$O complex
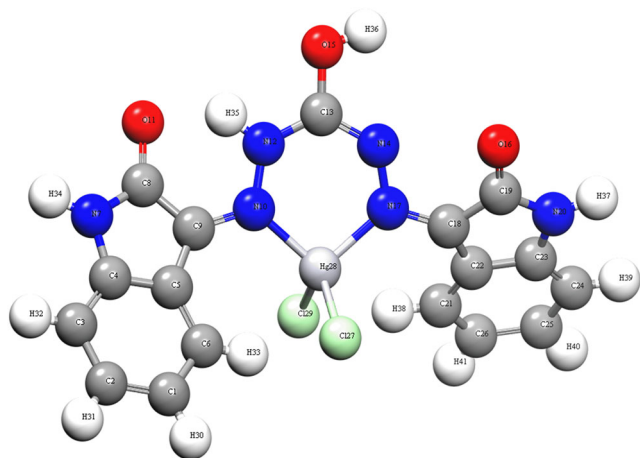
FIGURE 5 Molecular structure of [Hg(H$_3$L)(Cl)$_2$]·2H$_2$O complex

Antibacterial activity

The antibacterial activity of the examined compounds was performed by employing the agar diffusion technique.[31] Gram (+) *B. subtilis* and *S. aureus* and Gram (−) *E. coli* and *P. aeruginosa* clinical bacterial breeds were used in performing the antibacterial assay. The agar's surface was vaccinated with the bacteria culture, and then, the ligand and metal complexes are dissolved in DMSO.[32] The ligand and metal complexes were added to the bacteria culture and allowed to stand for about 1 h. Then, the plates were left at room temperature for 2 days. Then, the diameter of the inhibitory zones was measured (mm) which indicates the antibacterial activity of the tested compounds.

Antifungal activity

In vitro antifungal activity of the ligand and its metal complexes was screened by employing the disc diffusion method.[33] *C. albicans* microbe was used in performing the test for the ligand, and its metal complexes were dissolved in DMSO, negative control, (1 mg ml^{-1}). The incubation of the plates was left at room temperature for 2 days. The average diameter of inhibition regions of fungal growth was measured (in mm).

2.5.2 | Antioxidant activity

SOD-like activity

The reported method[34] was used to perform the SOD-like activity of the isolated compounds which were dissolved in DMSO, and for benchmarking studies, L-ascorbic acid activity has been specified.

ABTS free radical assay

Antioxidant activity was determined using (ABTS) free radical cation delocalization assay using the reported spectrophotometric method.[35,36]

3 | RESULTS AND DISCUSSIONS

Table S1 epitomizes the molecular formula, elemental analyses, and some of the physical characteristics for H$_3$L ligand and its complexes. The yielded complexes are non-hygroscopic and insoluble in water and outsmart solvents but soluble in DMSO. The molar conductivity of all complexes lies in 10–21 Ω^{-1}cm^2 mol^{-1} which indicates their nonelectrolytic character.[37,38]

3.1 | FT-IR spectra

Assignment of the IR principal bands of the ligand (Figure S1) and its complexes (Figures S2–S5) are depicted in Table S2. The IR spectrum of free H$_3$L ligand exhibits bands at 3347 and 3143 cm^{-1} attributable to v(NH)$_{charbohydrazone}$ and v(NH)$_{isatin}$, respectively. Two bands were observed at 1756 and 1728 cm^{-1}, characteristic for v(C=O)$_{charbohydrazone}$ and v(C=O)$_{isatin}$,

respectively. Furthermore, the spectrum demonstrates bands at 1614 and 1041 cm^{-1} attributable to the newly formed v(C=N)$_{azomethine}$ and v(N—N) vibrations. The bands display at 1507, 1470, 1345, and 1231 cm^{-1}, which are characteristics for δ(NH)$_{carbohydrazone}$, δ(NH)$_{isatin}$, v(C—N)$_{isatin}$, and v(C—N)$_{carbohydrazone}$, respectively. The *keto/enol* form in the solid state is possible which may have asserted by the appearance of bands at 3488 and 1185 cm^{-1} referring to new v(OH) and v(C—O), respectively.[39] The spectral data for metal chelates in comparison with those of the free ligand revealed that the H$_3$L ligand behaves in different manners towards different metal ions; this is confirmed by the following observations:

1. The shift of v(C=N)$_{azomethine}$ and v(N—N) bands to a higher wavenumber in all complexes concerning the free ligand indicates its participation in coordination to the metal ions.
2. For complexes [Cu(H$_2$L)(OAc)]·2H$_2$O, [Cd(H$_2$L)$_2$]·H$_2$O, and [Hg(H$_3$L)(Cl)$_2$]·2H$_2$O, the absence of band at 1756 cm^{-1} with the emergence of new bands at 1648, 1550, and 1694 cm^{-1} characteristic for newly formed azomethine group suggests enolization of (C=O)$_{charbohydrazone}$, whereas in [Fe(HL)(Cl)]·2H$_2$O complex, the disappearance of band at 1728 cm^{-1} with the appearance of the band at 1695 cm^{-1} suggests enolization of (C=O)$_{isatin}$.
3. For diamagnetic d^{10} complexes of Cd(II) and Hg(II), the existence of band at 1728 cm^{-1} distinctive for v(C=O)$_{isatin}$ confirms that isatin carbonyl groups in H$_3$L ligand are out of coordination to Cd(II) and Hg(II) ions.
4. For [Cu(H$_2$L)(OAc)]·2H$_2$O complex, the shift of v(C=O)$_{isatin}$ to a lower wavenumber confirms its participation in the chelation process to Cu(II) ions, whereas in [Fe(HL)(Cl)]·2H$_2$O complex, the shift of v(C=O)$_{carbohydrazone}$ confirms its participation in coordination to Fe(III) ions.
5. Finally, for [Cu(H$_2$L)(OAc)]·2H$_2$O complex, the new bands observed at 1562–1550 and 1446–1436 cm^{-1} were attributed to v_{as}(OAc) and v_s(OAc) vibrations, respectively. The monodentate stamp of acetate group was suggested by the difference between these two bands ($\Delta v = 116$ cm^{-1}).[40]

3.2 | ^{1}H NMR and ^{13}C NMR spectral studies

The existence of H$_3$L ligand in different forms is illustrated by the ^{1}HNMR spectrum (Figure S6). It can be illustrated by the existence of a signal at 13.36 ppm assignable to OH proton and the signals at 11.17, 10.84, 10.75, and 10.24 ppm which are assignable to NH protons of the *anti-* and *syn-*conforms. All the previous signals disappear on the addition of D$_2$O (Figure S7). The signals of aromatic protons of the benzene ring were observed between 6.85 and 8.13 ppm. Moreover, the suggested structure of H$_3$L was also confirmed by its ^{13}C NMR spectrum, which was recorded in DMSO-d_6 as a solvent, in which the carbon atoms of (—C$_8$=O), (—C$_{13}$=O), (—C$_9$=N), and (—C$_{13}$—O)$_{enolic}$ were displayed at 164.92, 162.98, 143.39, and 111.32 ppm, respectively, and the other aromatic carbon signals were observed at 152.61, 144.19, 133.06, 126.01, 122.37, and 115.67 ppm (Figure S8). In the ^{1}H NMR spectrum of [Cd(H$_2$L)$_2$]·H$_2$O complex (Figure S9), the presence of a signal at 10.50 ppm confirms that the (NH)$_{isatin}$ is out of complexation, and the demise of signals at 11.17, 10.84, and 10.24 ppm with the shift of δ(NH)$_{carbohydrazone}$ signal to 7.00 ppm suggests enolization of (C=O)$_{charbohydrazone}$ and coordination of ligand to Cd(II) ions through the deprotonated (OH)$_{enolic}$. All these signals disappear on deuteration (Figure S10). The ^{1}H NMR spectrum of [Hg(H$_3$L)(Cl)$_2$]·2H$_2$O complex (Figure S11), the presence of signals at 12.92 ppm confirms the enolization of (C=O)$_{carbohydrazone}$ and that it is not involved in coordination. The signal at 10.52 ppm assignable (NH)$_{isatin}$ protons confirms that the (NH)$_{isatin}$ is not involved in chelation. Furthermore, the remaining (NH)$_{charbohydrazone}$ signals shifted to the upper field region which disappear on deuteration (Figure S12) confirming the suggested coordination pattern in these complexes.

3.3 | Electronic spectra

UV-Vis spectrum of H$_3$L ligand (Figure S13) shows a peak at 272 nm due to $\pi \rightarrow \pi^*$ transitions in the benzene ring, a peak at 322 nm is due to $\pi \rightarrow \pi^*$ transitions in azomethine, whereas peaks at 392, 440, and 574 nm belong to $\pi \rightarrow \pi^*$ in (C=O), n $\rightarrow \pi^*$ in C=N, and C=O, respectively.[1] The electronic spectrum of [Fe(HL)(Cl)]·2H$_2$O complex (Figure S14) emerges three bands located at 546, 514, and 400 nm assignable to $^6A_{1g} \rightarrow {}^4T_{1g}$(G), $^6A_{ig} \rightarrow {}^4T_{2g}$(G), and $^6A_{ig} \rightarrow {}^4E_g$(G) transitions, respectively, characteristic for an octahedral structure environment around Fe(III) ion.[41,42] The magnetic moment value 5.81 BM is further support for the suggested geometry of the Fe(III) complex, whereas the electronic spectrum of [Cu(H$_2$L)(OAc)]·2H$_2$O complex (Figure S15) displays bands at 770, 564, and 284 nm attributable to $^2B_{1g} \rightarrow {}^2E_g$, $^2B_{1g} \rightarrow {}^2B_{2g}$, and $^2B_{1g} \rightarrow {}^2A_{2g}$.[43] Furthermore, the magnetic moment value is 1.98 BM which is close to μ_s value. The spectrum of [Cd(H$_2$L)$_2$]·H$_2$O

complex (Figure S16) exhibits a slight alteration in the energies of bands due to the $\pi \to \pi^*$ and $n \to \pi^*$ transitions. Also, the broad band located at 431 nm may be due to LMCT. Except that the complex shows no appreciable energy absorptions, following the filled d-orbital configuration of the metal ion. Finally, the electronic spectrum of $[Hg(H_3L)(Cl)_2] \cdot 2H_2O$ complex (Figure S17) displays moderately intense broad bands in the region of 500–478 nm which may be due to LMCT.

3.4 | Mass spectral studies

The mass spectrum of H_3L ligand, $[Fe(HL)(Cl)] \cdot 2H_2O$, $[Cu(H_2L)(OAc)] \cdot 2H_2O$, $[Cd(H_2L)_2] \cdot H_2O$, and $[Hg(H_3L)(Cl)_2] \cdot 2H_2O$ complexes (Figures S18–S22) show molecular ion peaks at m/z: 348.01, 473.06, 506.14, 825.09, and 656.17, respectively, which are equivalent to their molecular weight. This confirms the proposed structures for H_3L ligand and its complexes. The different fragments of H_3L ligand (Figure S23) give peaks with intensities at various m/z values like at 329.54 (34.71%) ($C_{17}H_9N_6O_2$), 313.68 (24.68%) ($C_{17}H_9N_6O$), 169.81 (60.62%) ($C_9H_5N_4$), 129.15 (100%) ($C_8H_5N_2$), and 114.84 (31.40%) (C_8H_4N).

3.5 | ESR spectroscopy

The electron spin resonance (ESR) spectrum of $[Cu(H_2L)(OAc)] \cdot 2H_2O$ complex (Figure 6) was performed employing DPPH standard at room temperature. Table 1 demonstrates the various parameters obtained from the ESR spectrum. The values of $g_{||}$, $g_\perp$, and g_{iso} were found to be 2.0415, 2.2008, and 2.1477, respectively. The values of g tensors are greater than 2.0023, which indicates that the ground orbital is $dx^2 - y^2$.[44] The axial symmetry parameter (G), covalence of (in-plane) σ-bonding (α^2), covalence (in-plane) π-bonding (β^2), $^2K_{||}$, $^2K_\perp$, and f were obtained by utilizing the next equations:

$$G = \left(g_{||} - 2.00277\right)/(g_\perp - 2.00277),$$

$$\alpha^2 = \left(A_{||}/0.036\right) + \left(g_{||} - 2.00277\right) + 3/7(g_\perp - 2.00277) + 0.04,$$

$$\beta^2 = \left(g_{||} - 2.00277\right)E/\left(-8\lambda\alpha^2\right),$$

where λ (spin-orbit coupling) $= -828$ cm^{-1} for free copper ion and E (electronic transition energy) $= 17,745$ cm^{-1}.
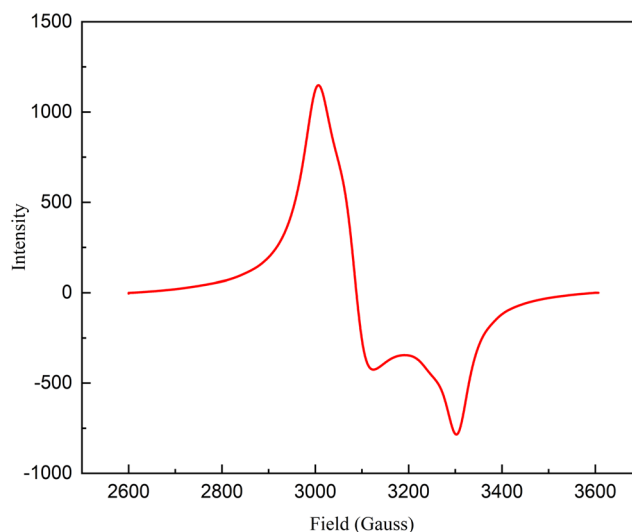
FIGURE 6 Electron spin resonance (ESR) spectrum of $[Cu(H_2L)(OAc)] \cdot 2H_2O$

$$^2K_{||} = \left(g_{||} - 2.00277\right)E/(8\lambda),$$

$$^2K_\perp = (g_\perp - 2.00277)E/(2\lambda),$$

$$^2K_{||} = \alpha^2 \times \beta^2,$$

$$f = g_{||}/A_{||}.$$

3.6 | Powder XRD studies

The X-ray diffraction (XRD) studies of the H_3L ligand, $[Fe(HL)(Cl)] \cdot 2H_2O$, $[Cu(H_2L)(OAc)] \cdot 2H_2O$, and $[Cd(H_2L)_2] \cdot H_2O$ complexes (Figure 7) were performed with the aid of X-ray diffractometer with Cu anode material, K-α[Å] $= 1.54060$. The lattice parameters were computed with the assistance of Qualx computer software.[45,46] The lattice parameters and volume are recorded together with Miller indices hkl in Table S3. The indexing was confirmed by comparing calculated and observed 2θ values. The powder XRD patterns of free ligand and its complexes are completely different emphasizing the successful coordination of the ligand with the metal ions. It is found that the H_3L ligand, $[Cu(H_2L)(OAc)] \cdot 2H_2O$ complex, and $[Cd(H_2L)_2] \cdot H_2O$ complex have triclinic structures,[47–49] whereas $[Fe(HL)(Cl)] \cdot 2H_2O$ complex has an orthorhombic structure.[50] The diffraction data were used for investigation of crystallite size, D, utilizing the *Scherrer equation*,[51] $D = 0.9\lambda/(\beta\cos\theta)$, where

TABLE 1 X-band electron spin resonance (ESR) spectrum of [Cu(H$_2$L)(OAc)]·2H$_2$O complex

$g_{||}$	$g_{\perp}$	g_{iso}	$A_{||}$ 10^{-4}	f	G	α^2	β^2	$^2K_{||}$	$^2K_{\perp}$
2.0415	2.2008	2.1477	121	168	0.1975	0.4997	0.2076	−0.1038	−2.122
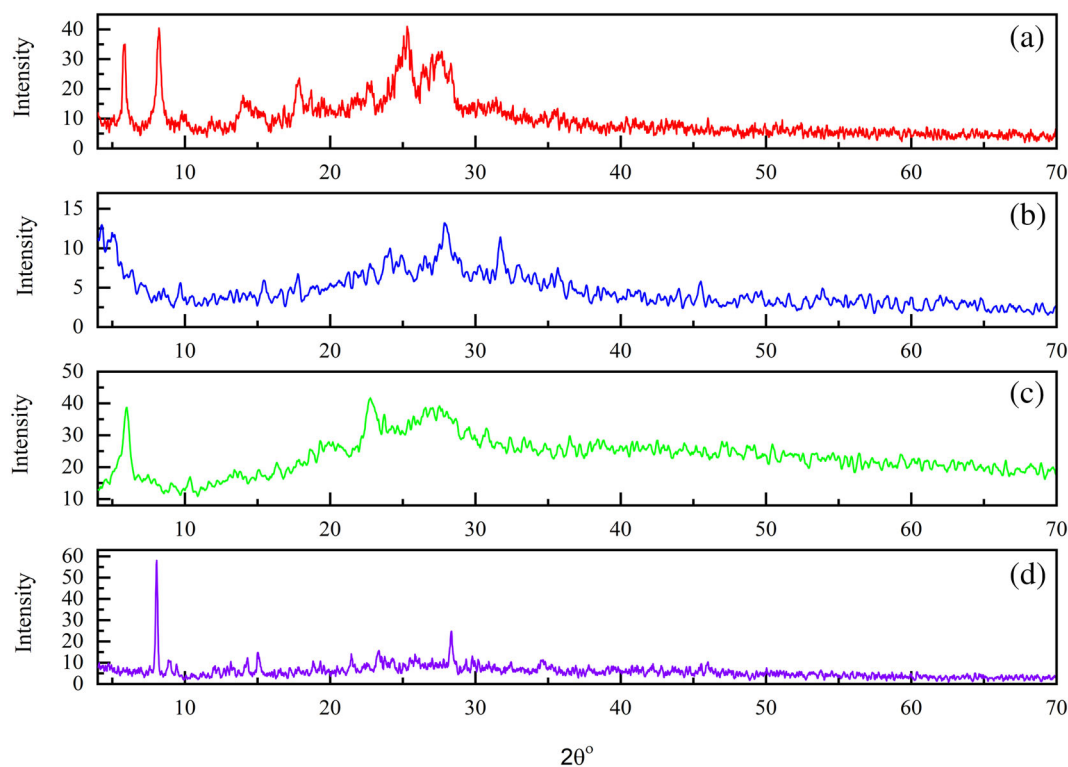
FIGURE 7 X-ray diffraction (XRD) graphs for (a) H$_3$L ligand, (b) [Fe(HL)(Cl)]·2H$_2$O, (c) [Cu(H$_2$L)(OAc)]·2H$_2$O, and (d) [Cd(H$_2$L)$_2$]· H$_2$O complexes

$\lambda = 1.5406$ Å, θ is Bragg diffraction angle, and β is the *FWHM* of the peak. The particle size for H$_3$L ligand, Fe(II), Cu(II), and Cd(II) complexes in accordance to the peak of the highest value of intensity equals 16.749, 14.103, 8.441, and 24.916 nm, respectively.[9]

3.7 | TGA and kinetic data

TGA of the metal complexes was carried out to investigate the weight loss percentage and to examine their thermal stability. The thermogram of the metal complexes (Figure S24) shows that upon heating, [Fe(HL)(Cl)]·2H$_2$O and [Hg(H$_3$L)(Cl)$_2$]·2H$_2$O complexes decompose in four steps whereas [Cu(H$_2$L)(OAc)]·2H$_2$O and [Cd(H$_2$L)$_2$]·H$_2$O complexes decompose in three and five steps, respectively. The step at the temperature range of 210°C to 280°C coordinated anions decomposes. The second to last steps are corresponding to the decay of organic moieties coordinated to the metal ions at the temperature scale of 280°C to 800°C (Table S4).[52] The

impact of the metal center on the thermal attitude of the complexes was studied utilizing Coats–Redfern[53,54] and Horowitz–Metzger[55] methods (Figures S25–S32). For [Fe(HL)(Cl)]·2H$_2$O complex, as an example, the first step of degradation occurs at 33°C to 131°C matching to loss of two water molecules with a weight loss of 7.53% (calc. 7.60%). The second step occurs at 132°C to 361°C, corresponding to the loss of HCl + C$_5$H$_5$N with a weight loss of 24.62% (calc. 24.42%). From 362°C to 793°C, the third step of decomposition takes place with a weight loss of 17.82% (calc. 17.55%) which matches with the loss of C$_2$HNO + N$_2$ molecules. The fourth step of thermal decomposition occurs at a temperature higher than 794°C by loss of FeO + HCN + CN + CH$_2$O + 7C fragments with weight loss of 50.43% (calc. 50.5%). The well-known Eyring equations[56,57] were used to estimate the kinetic and thermodynamic parameters. Data recorded in Tables S5 and S6 purposed that the decomposition steps are endothermic which was indicated by the positive value of ΔH^*. The majority of the degradation stages have a negative value for entropies (ΔS^*) clarifying

TABLE 2 Data of stability constant and free energy of complex Cd(OAc)$_2$ with H$_3$L

Milliliters added from M	[M]	Milliliters of L	[L]	$(E°)_M$	$(E°)_C$	$\Delta(E°)$ (mV)	j	log[L]	log β_{MX}	ΔG (kJ mol^{-1})
7	8.97×10^{-3}	2	2.56×10^{-3}	−0.92	−0.8485	−0.0715	0.3	−2.59	−0.468	2.67
7	8.4×10^{-3}	4	4.88×10^{-3}	−0.92	−0.875	−0.045	0.6	−2.31	0.56	−3.19
7	7.95×10^{-3}	7	7.95×10^{-3}	−0.92	−0.7845	−0.1355	1	−2.1	−0.19	1.09

the well-ordered activated complex than the reactants. Positive values of Gibbs free energy value (ΔG^*) indicate the nonspontaneous decomposition steps.

3.8 | Electrochemical behavior of Cd(OAc)$_2$ and HgCl$_2$ in presence of H$_3$L ligand

The chelation process between HgCl$_2$ and Cd(CH$_3$COO)$_2$ metal salts with H$_3$L ligand in DMSO were studied in 0.1 M KCl at 25°C and 1.2- to −1.4V potential window and scan rate 0.01, 0.02, 0.05, and 0.1 mV s^{-1} (Figures S33 and S34). It was observed that Hg(II) solution is an electroactive and reversible system with two-electron transfers (one electron in each step) as it emerges two anodic and two cathodic peaks (Hg(II)/Hg(I) and Hg(I)/Hg). Also, the data obtained from complexation between H$_3$L and Cd(II) show that the Cd(II) system is also reversible entails two-electron transfer (Cd(II)/Cd). The stability constant (β_{MX}) for both complexes for each addition, formal peak potential, and Gibbs free energy (ΔG) of the interaction of metal salt with H$_3$L (Tables 2 and 3) were calculated using the equations[58,59]:

$$\Delta E° = E°_C - E°_M = 2.303(RT/nF) * (\log \beta_{MX} + j \log C_x),$$

$$E° = (E_{Pa} + E_{Pc})/2,$$

$$\Delta G = -2.303\,RT \log \beta_{MX},$$

where $E°_M$ and $E°_C$ are the formal peak potential of the metal in lack and presence of H$_3$L, respectively; R is the universal gas constant; T is the absolute temperature, C_x is the H$_3$L concentration, and j is the coordination number of the complex.

3.9 | Fluorescence spectral studies

Stock solutions of H$_3$L ligand, Cu(OAc)$_2$, and Cd(OAc)$_2$·2H$_2$O salts were prepared in DMSO in 1.0×10^{-3} M concentrations. The stock solutions of the H$_3$L, Cd(II), and Cu(II) metal ions were further diluted to 6, 1.7–16, and 6.6–16 μM concentrations, respectively. The fluorescence spectrum of the free H$_3$L ligand emerges a broad emission signal at 566 nm after excitation at 480-nm wavelength (Figure 8). After the addition of Cd(II), a major raise (enhancement) in the emission intensity occurs. Also, the test was implemented out with a 1.7–16 μM concentration of

TABLE 3 Data of stability constant and free energy of complex $HgCl_2$ with H_3L

Milliliters added from M	[M]	Milliliters of L	[L]	$(E°)_M$	$(E°)_C$	$\Delta(E°)$ (mV)	j	log[L]	log β_{MX}	ΔG (kJ mol^{-1})
7	8.97×10^{-3}	2	2.56×10^{-3}	0.085	0.0875	−0.0025	0.3	−2.59	0.66	−3.74
7	8.4×10^{-3}	4	4.88×10^{-3}	0.085	0.089	−0.004	0.6	−2.31	1.19	−6.77
7	7.95×10^{-3}	7	7.95×10^{-3}	0.085	0.07325	0.01175	1	−2.1	2.49	−14.25

Cd(II) ions which yielded an important enhancement in the fluorescence spectrum of the ligand (Figure 8). The remarkable "turn-on" react is attributed to the linking of Cd(II) ion with the N and O atoms in the C=N and carbonyl groups, respectively. After coordination of Cd(II) with the ligand, the resulted molecule becomes puckered, which reduces the n → π* transition with a concomitant increase in π → π* transition. This lead to inhibition in the C=N isomerization resulting in chelation-enhanced fluorescence effect (CHEF).[60] The plot of emission intensity with the raised concentration of Cd(II) ion suggests that the H_3L ligand can be used for the quantitative analysis of Cd(II) ions in the aqueous solution. On the other hand, the emission spectrum of the ligand in the existence of Cu(II) ions was found to be quenched and the quenching increased by the increase in the Cu(II) ions concentration "6.6–16 μM concentration" (Figure 8). This conclusion may be clarified by the paramagnetic features of the Cu(II) ions "d^9" in which the unpaired d-orbital electrons effectively quench the singlets and triplets of the ligand.[61]

Binding constants were estimated utilizing the subsequent equation[62]:

$$\frac{1}{\Delta F} = \frac{1}{\Delta F_{max}} + \frac{1}{K_B \Delta F_{max}[M^{2+}]},$$

where ΔF: fluorescence intensity changes in the absence and presence of the metal ions ($F_x - F_o$), F_x: fluorescence intensity changes in presence of different concentrations of metal ions, F_o: fluorescence intensity changes in absence of metal ions, ΔF_{max}: maximum change in fluorescence of the ligand, K_B: binding constant, and $[M^{2+}]$: metal ion concentration.

The plot of $1/\Delta F$ and $1/[M^{2+}]$ was used to determine the binding constant (Figure S35) for Cd(II) and Cu(II) binding to H_3L ligand from the values of intercept and slope. The values of the binding constants for Cd(II) and Cu(II) to the ligand were found to be 3.79×10^4 and 2.04×10^4 M^{-1}, respectively. The formation of the 1:1 complex was also purposed from the linearity of the Benesi–Hildebrand plots.[63]

3.10 | DFT calculations

3.10.1 | Global chemical reactivity descriptions

Frontier molecular orbitals (Figures 9 and S36–S40) assess the electric optical properties, kinetic stability, and electronic transitions.[64] By using the energy gap chemical descriptors like electronegativity (χ), electrophilicity (ω),
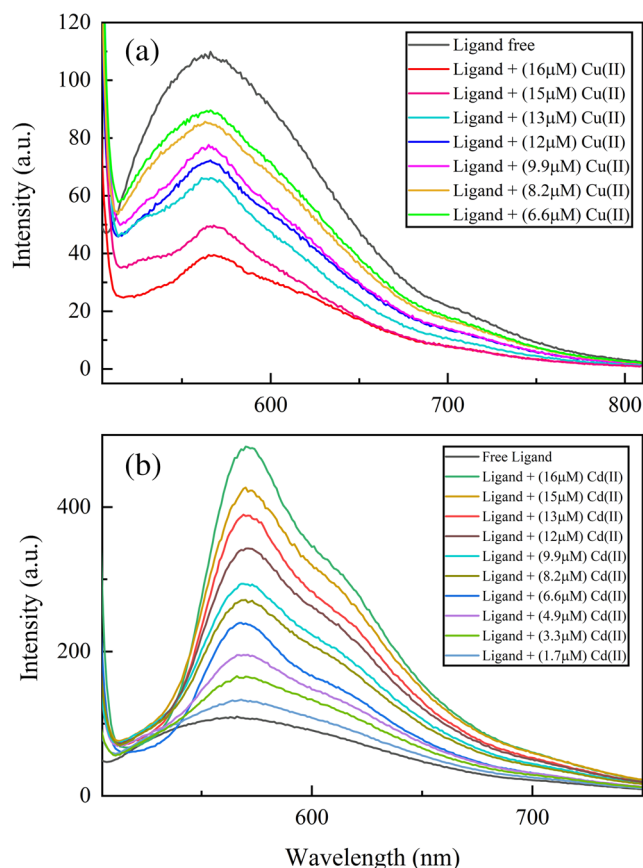
FIGURE 8 Fluorescence spectra of H_3L upon addition of (a) Cu(II) and (b) Cd(II) ions in DMSO

softness (S), chemical potential (μ), and hardness (η) for the compounds (Table 4) are calculated as follows[65–70]:

$$\chi = -\frac{1}{2}(E_{\text{LUMO}} + E_{\text{HOMO}}),$$

$$\mu = -\chi = \frac{1}{2}(E_{\text{LUMO}} + E_{\text{HOMO}}),$$

$$\eta = \frac{1}{2}(E_{\text{LUMO}} - E_{\text{HOMO}}),$$

$$S = \frac{1}{2}\eta,$$

$$\omega = \frac{\mu^2}{2\eta},$$

where HOMO is the highest occupied molecular orbital and LUMO is the lowest unoccupied molecular orbital.

Chemical potential (μ), which estimates the escaping capability of electrons from the equilibrium framework, increases according to the following order:

Cd(II) complex > H_3L ligand > Fe(III) complex > Hg(II) complex > Cu(II) complex.

3.10.2 | Geometry optimization

Molecular structures of H_3L and its complexes are outlined in Figures 1–5. Bond lengths and angles (Tables S7–S16) were screened to confirm the suggested structures. The bond angles of the H_3L ligand were changed on complex formations. The primary amendments are remarked on N(14)—C(13)—O(15), N(12)—C(13)—O(15), C(9)—N(10)—N(12), C(18)—N(17)—N(14), O(16)—C(19)—C(18), O(11)—N(7)—V(8), O(16)—C(19)—N(20), and O(11)—C(8)—C(9). The bond angles in complexes confirm the proposed octahedral environment (sp^3d^2 hybridization) around Fe(III), Cu(II), and Cd(II) metal ions. Moreover, The bond angles in Hg(II) complex confirm the tetrahedral environment with sp^3 hybridization.

3.10.3 | Molecular electrostatic potential

Electrostatic potential maps (Figures S41–S45) of the ligand and its metal complexes were obtained using density functional theory (DFT)/revising Perdew-Burke-Ernzerhof functional basis set. Electrostatic potential maps help in understanding the electrophilic and nucleophilic reactions. In the present work, molecular electrostatic potential (MEP) suggests different values of electrostatic potentials in the isolated molecules; the region in red color represents the electrophilic attack, whereas regions of blue color represent nucleophilic reaction. For example, H_3L ligand and its Hg(II) complex show negative regions at $O^{(11)}$, $O^{(15)}$, $O^{(16)}$, $N^{(10)}$, and $N^{(17)}$ atoms with negative values of (−0.531, −0.441, −0.530, −0.180, and −0.184 a.u.) and (−0.471, −0.407, −0.401, −0.208, and −0.280 a.u.), respectively, for ligand and Hg(II) complex. The most preferred sites for the electrophilic attack are $O^{(11)}$, and $O^{(16)}$. On the other hand, the positive regions locate at $C^{(13)}$, $C^{(8)}$, $C^{(19)}$, $C^{(4)}$, and $C^{(23)}$ with positive values (0.602, 0.459, 0.457, 0.269, and 0.268 a.u.) and (0.551, 0.391, 0.409, 0.248, and 0.248 a.u.), respectively, for ligand and Hg(II) complex. The most preferred site for the nucleophilic attack is $C^{(13)}$.

3.10.4 | Mulliken atomic charges

Calculated Mulliken atomic charges of H_3L ligand were given in Figure S46, whereas Tables S17–S20 give that of the metal chelates. We can conclude that the atoms with negative Mulliken atomic charges are recognized by their

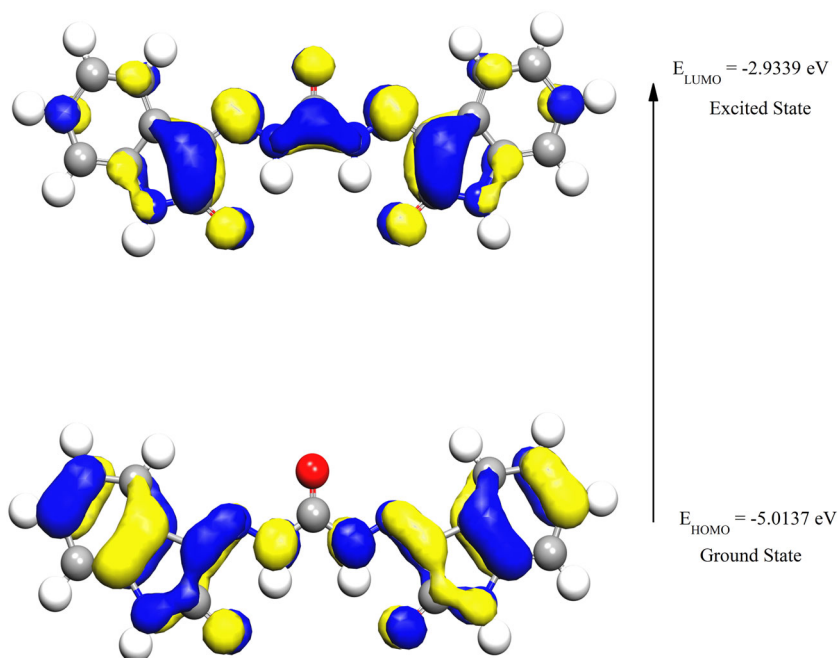**FIGURE 9** 3D plots frontier orbital energies using density functional theory (DFT) method for H_3L ligand

$E_{LUMO} = -2.9339 \text{ eV}$

Excited State

$E_{HOMO} = -5.0137 \text{ eV}$

Ground State

TABLE 4 Calculated E_H, E_L, energy band gap ($E_H - E_L$), chemical potential (μ), electronegativity (χ), global hardness (η), global softness (S), and global electrophilicity index (ω) for H_3L ligand and its metal complexes

Compound	E_H (eV)	E_L (eV)	$E_H - E_L$ (eV)	μ (eV)	χ (eV)	η (eV)	S (eV^{-1})	ω (eV)
H_3L	−5.01374	−2.93396	−2.07978	−3.97385	3.97385	1.03989	0.51994	7.59283
$[Fe(HL)(Cl)]\cdot 2H_2O$	−4.71414	−3.86486	−0.84927	−4.28951	4.28950	0.42464	0.21232	21.6654
$[Cu(H_2L)(OAc)]\cdot 2H_2O$	−8.33709	−6.83828	−1.49882	−7.58768	7.58768	0.74941	0.37470	38.4123
$[Cd(H_2L)_2]\cdot H_2O$	−4.35731	−3.24391	−1.11342	−3.80061	3.80062	0.55673	0.27842	12.9733
$[Hg(H_3L)(Cl)_2]\cdot 2H_2O$	−5.39007	−3.90895	−1.48113	−4.64951	4.64951	0.74056	0.37028	14.5956

donating features and vice versa. For example, for the H_3L ligand, all carbon atoms attached to hydrogens are of almost negative values. Carbon atoms attached to electronegative atoms are of positive charges, such as $C^{(13)}$ which has the highest positive atomic charge. Also, $O^{(11)}$, $O^{(15)}$, $O^{(16)}$, $N^{(10)}$, and $N^{(17)}$ are of a negative charge and more basic. The charge of $H^{(31)}$, $H^{(32)}$, $H^{(33)}$, and $H^{(34)}$ of the N–H groups are of high positive charge unlike, the remaining hydrogen atoms.

3.11 | Biological screening and molecular docking

3.11.1 | Antimicrobial activities

The antimicrobial activities of the H_3L ligand and its metal chelates (Figures S47–S51) were inspected against

different bacteria and fungi strains and listed in Table 5. The antimicrobial screening data revealed that:

1. All complexes show a considerable activity against *B. subtilis* and *E. coli* with inhibition regions of diameters ranging between 8 and 30 mm.
2. The antimicrobial behavior of the complexes with superior activities than that of H_3L ligand could be explained by the chelation theory[71] which states that the partial sharing of the metal charge with the ligand donor groups and the probability of π-electron delocalization over the chelate rings diminish the polarity of the metal ion, leading to rising in the lipophilic nature that facilities the permeation of the complex into the microorganism lipid membrane.
3. The order of rising activities of all compounds against each bacterial strain is *S. aureus*: $[Fe(HL)(Cl)]\cdot 2H_2O < H_3L < [Cd(H_2L)_2]\cdot H_2O < [Hg(H_3L)(Cl)_2]\cdot 2H_2O$;

TABLE 5 Inhibition zones diameter (in mm unit) of ligand and its complexes against different test targets

Sample	Bacillus subtilis	Staphylococcus aureus	Escherichia coli	Pseudomonas aeruginosa	Candida albicans
DMSO	−ve	10	−ve	−ve	−ve
H_3L	−ve	9	−ve	−ve	12
$[Fe(HL)(Cl)]\cdot 2H_2O$	8	7	14	−ve	−ve
$[Cu(H_2L)(OAc)]\cdot 2H_2O$	15	−ve	7	12	−ve
$[Cd(H_2L)_2]\cdot H_2O$	30	10	12	−ve	15
$[Hg(H_3L)(Cl)_2]\cdot 2H_2O$	17	20	8	8	8

B. subtilis: $[Fe(HL)(Cl)]\cdot 2H_2O < [Cu(H_2L)(OAc)]\cdot 2H_2O < [Hg(H_3L)(Cl)_2]\cdot 2H_2O < [Cd(H_2L)_2]\cdot H_2O$; *E. coli*: $[Cu(H_2L)(OAc)]\cdot 2H_2O < [Hg(H_3L)(Cl)_2]\cdot 2H_2O < [Cd(H_2L)_2]\cdot H_2O < [Fe(HL)(Cl)]\cdot 2H_2O$; *P. aeruginosa*: $[Hg(H_3L)(Cl)_2]\cdot 2H_2O < [Cu(H_2L)(OAc)]\cdot 2H_2O$.

4. The high activity Cd(II) complex is related to the overlap of metal orbitals with the orbitals of ligand moieties; this contributes to the extra distribution of the positive charge of the metal on the donor groups of the ligand. This lowers the polarity of the metal ion, which increases the resonance of π-electrons and the liposolubility of the whole chelate, resulting in a good diffusion of the metal complex into microbes.[72]

5. The antifungal studies concluded that the H_3L ligand, Hg(II), and Cd(II) metal complexes were active against *C. albicans* and possess a good potency. And the order of increasing antifungal activities is: $[Hg(H_3L)(Cl)_2]\cdot 2H_2O < H_3L < [Cd(H_2L)_2]\cdot H_2O$.

6. The inactivity of H_3L ligand and its metal complexes towards some of the microorganism strains may be associated with the chance of lipophobic nature of those compounds or the impedance and process of efflux pump developed by these bacteria that forestall these compounds from penetration of the lipid membrane.[73]

3.11.2 | SOD-like activity

The SOD-like attitude of ligand and its metal complexes was estimated by using their potential to lessen the reduction of NBT by superoxide ions formed by the xanthine/xanthine oxidase framework.[74] By calculation absorbance at 560 nm, the NBT reduction was followed spectrophotometrically. Because superoxide ions have a short half-life, they must be continuously generated. Thus, by converting xanthine and oxygen to uric acid and H_2O_2 to xanthine oxidase, superoxide ions are produced. Then, the NBT is converted to formazan by the action of

the superoxide. The metal complexes compete with NBT for the oxidation of the superoxide ions produced, and the lower the IC_{50}, the more efficient the metal complex; Table 6 shows the SOD-like activity of the tested compounds.

3.11.3 | ABTS free radical scavenging activity

All isolated compounds were examined for antioxidant activity using ABTS assay. The statements in Table 7

TABLE 6 SOD-like activity of the tested compounds

Sample	Δ through 5 min	% inhibition
DMSO	0.48	0
L-Ascorbic acid	0.099	79.38
H_3L	0.357	25.63
$[Fe(HL)(Cl)]\cdot 2H_2O$	0.372	22.50
$[Cu(H_2L)(OAc)]\cdot 2H_2O$	0.381	20.63
$[Cd(H_2L)_2]\cdot H_2O$	0.324	32.51
$[Hg(H_3L)(Cl)_2]\cdot 2H_2O$	0.397	17.29

$$\%\text{inhibition} = \frac{(\Delta\,\text{control} - \Delta\,\text{test})}{(\Delta\,\text{control})} \times 100$$

TABLE 7 ABTS scavenging activity of H_3L and its metal chelates

Sample	Absorbance	% ABTS inhibition
DMSO	0.527	0
L-Ascorbic acid	0.018	96.58
H_3L	0.416	21.06
$[Fe(HL)(Cl)]\cdot 2H_2O$	0.435	17.46
$[Cu(H_2L)(OAc)]\cdot 2H_2O$	0.427	18.96
$[Cd(H_2L)_2]\cdot H_2O$	0.372	29.41
$[Hg(H_3L)(Cl)_2]\cdot 2H_2O$	0.458	13.09

showed that the complexes have the highest scavenging effect with ABTS free radical is arranged according to the following order Cd(II) complex > H_3L ligand > Cu (II) complex > Fe(III) complex > Hg(II) complex.

3.11.4 | Molecular docking

Molecular docking was performed and the best docking scores between H_3L ligand and its complexes with targets are incorporated in Table 8.

Molecular docking results showed that:

1. H_3L ligand showed the highest ability of binding to *S. aureus* (Figure 10) with a binding energy of -8.9 kcal mol^{-1}. In this binding mode, five conventional H-bonds are observed: $O_{(16)} \longrightarrow (NH) ARG^{192}$ (3.03 Å), $N_{(20)}H_{(34)} \longrightarrow (O) SER^{75}$ (2.19 Å), $O_{(16)} \longrightarrow (NH) SER^{75}$ (2.99 Å), $N_{(14)}H_{(33)} \longrightarrow (O) GLU^{173}$ (2.39 Å), and $N_{(17)} \longrightarrow (NH) MET^{172}$ (2.09 Å).

2. [Fe(HL)(Cl)]·2H$_2$O complex displays the highest binding abilities in binding with *E. coli* (Figure 11) and *P. aeruginosa* with a binding energy of -10.18 and -9.44 kcal mol^{-1}, respectively, when compared with other complexes.

3. [Cu(H$_2$L)(OAc)]·2H$_2$O complex shows the binding energy of -9.37 kcal mol^{-1} with *E. coli* target (Figure 12).

4. [Cd(H$_2$L)$_2$]·H$_2$O complex binds to *B. subtilis* and xanthine oxidase (Figure S52) targets with a binding energy of -7.36 and -8.37 kcal mol^{-1}, respectively.

5. [Hg(H$_3$L)(Cl)$_2$]·2H$_2$O complex binds with all targets (Figure S53) with energy ranging between -7.2 and -8.17 kcal mol^{-1}.

6. The data obtained from docking studies match with the experimental data to some extent. For example, Fe(III) complex shows the highest activity against *E. coli* with an inhibition region of 14 mm and gives the best docking score to the *E. coli* target (10.18 kcal mol^{-1}). The mismatch between docking and experimental data results from the dependence of

TABLE 8 Binding free energy of H_3L ligand and its metal complexes with different targets obtained from docking using *Auto-Dock 4.2*

Compound/target	Escherichia coli	Pseudomonas aeruginosa	Staphylococcus aureus	Bacillus subtilis	Candida albicans	Xanthine oxidase
H_3L	-9.59	-9.3	-8.9	-7.4	-8.69	-8.07
[Fe(HL)(Cl)]·2H$_2$O	-10.18	-9.44	-8.61	-8.34	-7.86	-8.24
[Cu(H$_2$L)(OAc)]·2H$_2$O	-9.37	-9.33	-7.68	-8.16	-8.24	-8.16
[Cd(H$_2$L)$_2$]·H$_2$O	-9.45	-8.98	-8.66	-7.36	-10.55	-8.37
[Hg(H$_3$L)(Cl)$_2$]·2H$_2$O	-8.17	-7.93	-7.73	-7.2	-7.8	-8.15

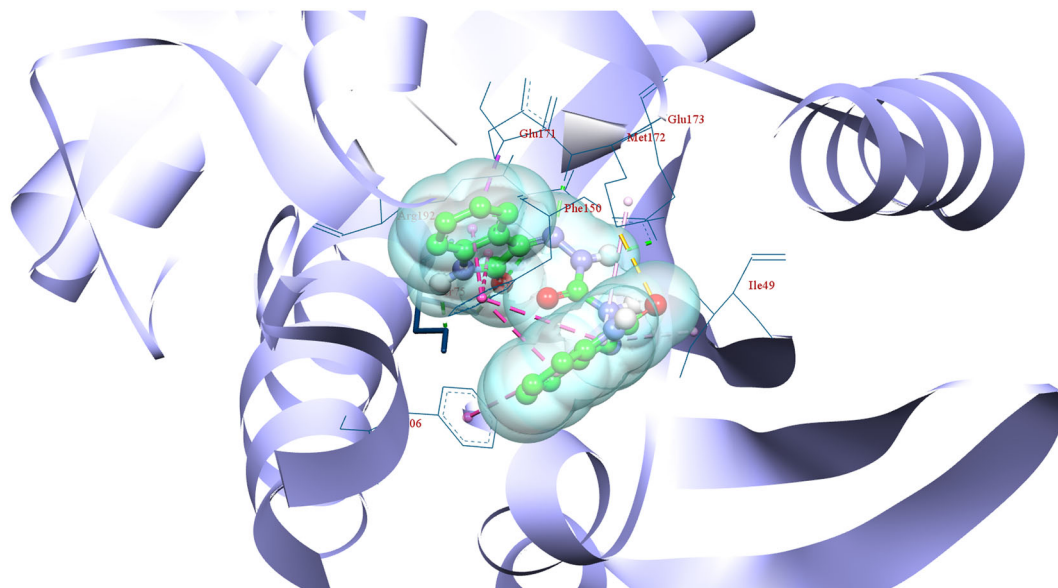**FIGURE 10** 3D molecular interactions of H_3L ligand to *Staphylococcus aureus*
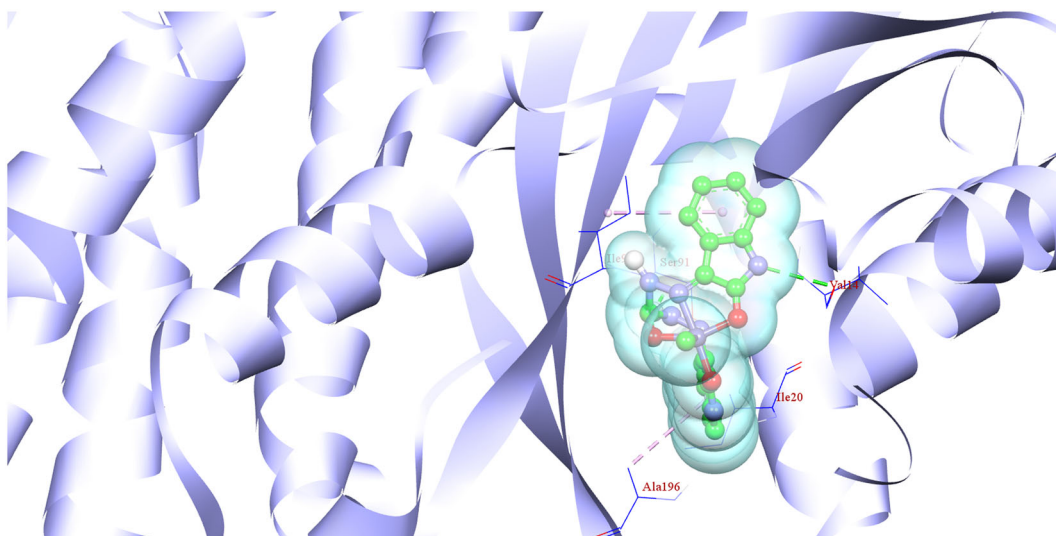
FIGURE 11 3D molecular interactions of [Fe(HL)(Cl)]·2H$_2$O complex to *Escherichia coli*
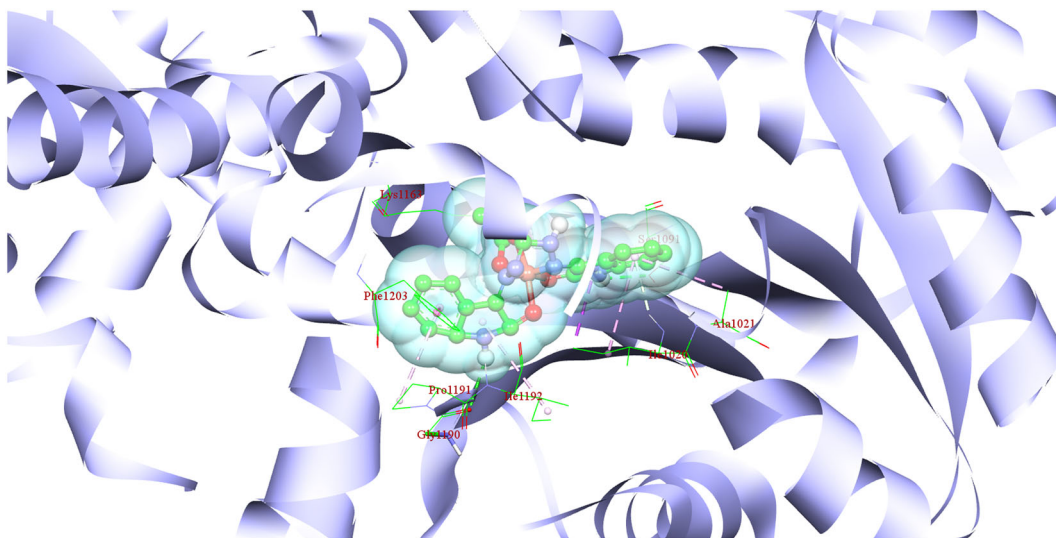
FIGURE 12 3D molecular interactions of [Cu(H$_2$L)(OAc)]·2H$_2$O complex to *Escherichia coli*

docking on scoring functions and algorithms, besides its sensitivity to the active sites under investigation. On the other hand, it does not take into account the experimental factors such as physicochemical properties of the drug (size, concentration, and pKa), properties of the membrane (thickness, area, solution pH, and permeability for the drug), and mechanism of the drug transport.[75,76]

7. It was also remarked the fine binding affinity in interaction with the binding site residues implying van der Waals interactions, conventional H-bonding and π-interactions, π-alkyl, and π-sulfur.

4 | CONCLUSION

A series of Fe(III), Cu(II), Cd(II), and Hg(II) complexes of H$_3$L ligand have been synthesized and characterized by different spectroscopic techniques. Geometry optimization MEP and chemical reactivity of these compounds are performed using the DFT method. The experimental IR spectra were compared with the theoretical values. Powder XRD data revealed that the ligand and its complexes have a semicrystalline character. The shift of anodic and cathodic current and potential in cyclic voltammetry estimates the successful coordination

between the ligand with Cd(II) and Hg(II) metal ions. Furthermore, the ligand shows a fluorescence spectrum that was quenched upon chelation with Cu(II) metal and was enhanced upon coordination with Cd(II) metal. The antimicrobial and antioxidant activities were estimated and showed that the isolated compounds biological activities to some extent. A molecular docking study of the ligand and its metal chelates was performed based on the protein structure together with the structural data of the tested compounds and has provided precious information about the binding attitude and the affinity of these compounds towards different strains.

AUTHOR CONTRIBUTIONS

Adel Younis: Methodology; software. **Mohammed El-Gamil:** Software. **T. H. Rakha:** Conceptualization; supervision. **Gaber Abu El-Reash:** Conceptualization; formal analysis; software; supervision.

DATA AVAILABILITY STATEMENT

The data that supports the findings of this study are available in the supplementary material of this article.

ORCID

Adel M. Younis https://orcid.org/0000-0003-4056-0718
Mohammed M. El-Gamil https://orcid.org/0000-0001-5605-2844
Tawfik H. Rakha https://orcid.org/0000-0001-9787-8482
Gaber M. Abu El-Reash https://orcid.org/0000-0002-0456-7325

REFERENCES

[1] B. Kurt, H. Temel, M. Atlan, S. Kaya, *J. Mol. Struct.* **2020**, *1209*, 127928.

[2] H. Schiff, *Eur. J. Org. Chem.* **1869**, *150*, 193.

[3] E. N. Md Yusof, T. B. S. A. Ravoof, E. R. Tiekink, A. Veerakumarasivam, K. A. Crouse, M. I. Mohamed Tahir, H. Ahmad, *Int. J. Mol. Sci.* **2015**, *16*, 11034.

[4] G. A. A. Al-Hazmi, K. S. Abou-Melha, N. M. El-Metwaly, I. Althagafi, F. Shaaban, M. G. Elghalban, M. M. El-Gamil, *Appl. Organomet. Chem.* **2019**, *34*, e5408.

[5] V. Angelova, V. Karabeliov, P. A. Andreeva-Gateva, J. Tchekalarova, *Drug Dev. Res.* **2016**, *77*, 379.

[6] O. E. Sherif, N. S. Abdel-Kader, *Arab. J. Chem.* **2018**, *11*, 700.

[7] A. M. Abu-Dief, I. M. A. Mohamed, *Beni Suef Univ. J. Basic Appl. Sci.* **2015**, *4*, 119.

[8] Y. Harinath, D. H. Kumar Reddy, B. N. Kumar, C. Apparao, K. Seshaiah, *Spectrochim. Acta A Mol. Biomol. Spectrosc.* **2013**, *101*, 264.

[9] S. M. El-Megharbel, R. Z. Hamza, M. S. Refat, *Chem.-Biol. Interact.* **2014**, *220*, 169.

[10] M. S. More, P. G. Joshi, Y. K. Mishra, P. K. Khanna, *Mater. Today Chem.* **2019**, *14*, 100195.

[11] M. A. Zayed, A. Belal, S. M. A. H. Ragha, *J. Transit. Met. Complexes* **2018**, *1*, 1.

[12] C. R. Prakash, S. Raja, J. Saudi, *Chem. Soc.* **2013**, *17*, 337.

[13] O. A. Dar, S. A. Lone, M. A. Malik, F. M. Aqlan, M. Y. Wani, A. A. Hashmi, A. Ahmad, *Heliyon* **2019**, *5*, e02055.

[14] A. I. Vogel, J. Bassett, J. Bassett, *Vogel's Textbook of Quantitative Inorganic Analysis: Including Elementary Instrumental Analysis*, Longman **1978**.

[15] B. Delley, *J. Chem. Phys.* **1990**, *92*, 508.

[16] B. Delley, *J. Chem. Phys.* **2000**, *113*, 7756.

[17] K. Prasanth, R. S. Pillai, S. A. Peter, H. Bajaj, R. Jasra, H. Chung, T. Kim, S. Song, *J. Alloys Compd.* **2008**, *466*, 439.

[18] X. Wu, A. K. Ray, *Phys. Rev. B* **2002**, *65*, 085403.

[19] Modeling and Simulation Solutions for Chemicals and Materials Research. : BIOVIA Materials Studio, Accelrys Software Inc., San Diego, USA, **2017**.

[20] A. Matveev, M. Staufer, M. Mayer, N. Rösch, *Int. J. Quantum Chem.* **1999**, *75*, 863.

[21] B. Hammer, L. B. Hansen, J. K. Nørskov, *Phys. Rev. B* **1999**, *59*, 7413.

[22] G. M. Morris, R. Huey, W. Lindstrom, M. F. Sanner, R. K. Belew, D. S. Goodsell, A. J. Olson, *J. Comput. Chem.* **2009**, *30*, 2785.

[23] M. F. Sanner, *J. Mol. Graphics Modell.* **1999**, *17*, 57.

[24] X. Qiu, S. S. Abdel-Meguid, C. A. Janson, R. I. Court, M. G. Smyth, D. J. Payne, *Protein Sci.* **1999**, *8*, 2529.

[25] S. Zimmermann, S. Pfennig, P. Neumann, H. Yonus, U. Weininger, M. Kovermann, J. Balbach, M. T. Stubbs, *FEBS Lett.* **2015**, *589*, 2283.

[26] K. K. W. Siu, J. E. Lee, G. D. Smith, C. Horvatin-Mrakovcic, P. L. Howell, *Acta Crystallogr. Sect. F Struct. Biol. Cryst. Commun.* **2008**, 64.

[27] C.-J. Lee, X. Liang, X. Chen, D. Zeng, S. H. Joo, H. S. Chung, A. W. Barb, S. M. Swanson, R. A. Nicholas, Y. Li, E. J. Toone, C. R. H. Raetz, P. Zhou, *Chem. Biol.* **2011**, *18*, 38.

[28] M. V. Keniya, M. Sabherwal, R. K. Wilson, M. A. Woods, A. A. Sagatova, J. D. A. Tyndall, B. C. Monk, *Antimicrob. Agents Chemother.* **2018**, *62*, e01134.

[29] C. Enroth, B. T. Eger, K. Okamoto, T. Nishino, T. Nishino, E. F. Pai, *Proc. Natl. Acad. Sci.* **2000**, *97*, 10723.

[30] Dassault Systèmes BIOVIA. Visualizer, Dassault Systèmes, San Diego, USA, **2019**.

[31] O. A. El-Gammal, G. M. A. El-Reash, R. A. Bedier, *Appl. Organomet. Chem.* **2019**, *33*, e5141.

[32] G. Verma, A. Marella, M. Shaquiquzzaman, M. Akhtar, M. R. Ali, M. M. Alam, *J. Pharm. Bioallied Sci.* **2014**, *6*, 69.

[33] A. C. Ekennia, D. C. Onwudiwe, A. A. Osowole, L. O. Olasunkanmi, E. E. Ebenso, *J. Chemom.* **2016**, *2016*, 1.

[34] S. M. Bridges, M. L. Salin, *J. Plant Physiol.* **1981**, *68*, 275.

[35] M. A. Al-Omair, A. R. Sayed, M. M. Youssef, *Molecules* **2018**, *23*, 1133.

[36] R. Re, N. Pellegrini, A. Proteggente, A. Pannala, M. Yang, C. Rice-Evans, *Free Radical Biol. Med.* **1999**, *26*, 1231.

[37] W. J. Geary, *Coord. Chem. Rev.* **1971**, *7*, 81.

[38] S. M. El-Megharbel, R. Z. Hamza, M. S. Refat, *Spectrochim. Acta A Mol. Biomol. Spectrosc.* **2014**, *131*, 534.

[39] A. M. A. Adam, T. A. Altalhi, S. M. El-Megharbel, H. A. Saad, M. S. Refat, I. Grabchev, R. A. Althobaiti, *Inorg. Chem. Commun.* **2021**, *124*, 108408.

[40] O. A. El-Gammal, G. M. Abu El-Reash, S. E. Ghazy, A. H. Radwan, *J. Mol. Struct.* **2012**, *1020*, 6.

[41] S. H. Rahaman, H. Chowdhury, D. Bose, R. Ghosh, C.-H. Hung, B. K. Ghosh, *Polyhedron* **2005**, *24*, 1755.

[42] S. Sarkar, K. Dey, *Spectrochim. Acta A Mol. Biomol. Spectrosc.* **2005**, *62*, 383.

[43] V. D. Biradar, B. H. Mruthyunjayaswamy, *Sci. World J.* **2013**, *2013*, 451629.

[44] A. Fetoh, M. A. Mohammed, M. M. Youssef, G. M. Abu El-Reash, *J. Mol. Liq.* **2019**, *287*.

[45] A. Altomare, N. Corriero, C. Cuocci, A. Falcicchio, A. Moliterni, R. Rizzi, *J. Appl. Crystallogr.* **2015**, *48*, 598.

[46] A. Altomare, C. Cuocci, C. Giacovazzo, A. Moliterni, R. Rizzi, *J. Appl. Crystallogr.* **2008**, *41*, 815.

[47] P. A. Abramov, T. P. Zemerova, N. K. Moroz, N. B. Kompankov, A. A. Zhdanov, A. R. Tsygankova, C. Vicent, M. N. Sokolov, *Inorg. Chem.* **2016**, *55*, 1381.

[48] J. Gao, J. Yan, S. Beeg, D.-L. Long, L. Cronin, *J. Am. Chem. Soc.* **2013**, *135*, 1796.

[49] E. Janusson, N. de Kler, L. Vila-Nadal, D. L. Long, L. Cronin, *Chem. Comm.* **2019**, *55*, 5797.

[50] K. Uehara, T. Miyachi, N. Mizuno, *Inorg. Chem.* **2014**, *53*, 5341.

[51] A. M. Naglah, M. A. Al-Omar, A. Kalmouch, A. A. Gobouri, S. H. Abdel-Hafez, S. M. El-Megharbel, M. S. Refat, *Russ. J. Gen. Chem.* **2019**, *89*, 1702.

[52] S. Gautam, S. Chandra, H. Rajor, S. Agrawal, P. K. Tomar, *Appl. Organomet. Chem.* **2018**, *32*, e3915.

[53] A. W. Coats, J. Redfern, *Nature* **1964**, *201*, 68.

[54] A. M. A. Adam, T. A. Altalhi, S. M. El-Megharbel, H. A. Saad, M. S. Refat, I. Grabchev, R. A. Althobaiti, *Russ. J. Gen. Chem.* **2020**, *90*, 2394.

[55] H. H. Horowitz, G. Metzger, *J. Anal. Chem.* **1963**, *35*, 1464.

[56] A. Frost, R. Pearson, *J. Phys. Chem.* **1961**, *65*, 384.

[57] T. Hatakeyama, F. Quinn, *Thermal Analysis: Fundamentals and Applications to Polymer Science, [sl]*, John Wiley & Sons, New York **1999**.

[58] D. A. C. Brownson, C. E. Banks, V. Springer, *The Handbook of Graphene Electrochemistry*, Springer **2014**.

[59] A. Fetoh, M. A. Mohammed, M. M. Youssef, G. M. Abu El-Reash, *Appl. Organomet. Chem.* **2019**, *33*, e4787.

[60] S. Zehra, R. A. Khan, A. Alsalme, S. Tabassum, *J. Fluoresc.* **2019**, *29*, 1029.

[61] M. D. P. De Costa, W. A. P. A. Jayasinghe, *J. Photochem, Photobiol. A* **2004**, *162*, 591.

[62] H. A. Benesi, J. H. Hildebrand, *J. Am. Chem. Soc.* **1949**, *71*, 2703.

[63] A. Sahu, N. Kasoju, U. Bora, *Biomacromolecules* **2008**, *9*, 2905.

[64] K. Fukui, T. Yonezawa, C. Nagata, H. Shingu, *J. Chem. Phys.* **1954**, *22*, 1433.

[65] J. Janak, *Phys. Rev. B* **1978**, *18*, 7165.

[66] R. G. Parr, Density functional theory of atoms and molecules, in *Horizons of Quantum Chemistry*, Springer **1980** 5.

[67] R. G. Parr, L. Szentpaly, S. Liu, *J. Am. Chem. Soc.* **1999**, *121*, 1922.

[68] J. P. Perdew, R. G. Parr, M. Levy, J. L. Balduz Jr., *Phys. Rev. Lett.* **1982**, *49*, 1691.

[69] T. A. Yousef, G. M. A. El-Reash, R. M. El Morshedy, *Polyhedron* **2012**, *45*, 71.

[70] T. A. Yousef, G. M. Abu El-Reash, R. M. El Morshedy, *J. Mol. Struct.* **2013**, *1045*, 145.

[71] S. M. El-Megharbel, N. M. El-Metwaly, M. S. Refat, *Spectrochim. Acta A Mol. Biomol. Spectrosc.* **2015**, *149*, 263.

[72] M. Montazerozohori, M. Nasr-Esfahani, M. Hoseinpour, A. Naghiha, S. Zahedi, *Chem. Speciation Bioavailability* **2014**, *26*, 240.

[73] M. Sunitha, P. Jogi, B. Ushaiah, C. G. Kumari, *E- J. Chem.* **2012**, *9*, 287909.

[74] C. J. Weydert, J. J. Cullen, *Nat. Protoc.* **2010**, *5*, 51.

[75] S.-Y. Huang, X. Zou, *Int. J. Mol. Sci.* **2010**, *11*, 3016.

[76] S. Sarfaraz, I. Muneer, H. Liu, *J. Comput.-Aided Mol. Des.* **2020**, *34*, 1237.

SUPPORTING INFORMATION

Additional supporting information may be found online in the Supporting Information section at the end of this article.